Applied Thermal Engineering, Volume 242, April 2024, Article number 122410
DOI:10.1016/j.applthermaleng.2024.122410

Metal Foam Recuperators on Micro Gas Turbines: Multi-Objective Optimisation of Efficiency, Power and Weight

Panagiota Chatzi[a], Theofilos Efstathiadis[a], Alex A. Skordos[b], Anestis I. Kalfas[a]

a: Laboratory of Fluid Mechanics and Turbomachinery, Aristotle University of Thessaloniki, Thessaloniki 54124, Greece
b: Composites and Advanced Materials Centre, Cranfield University, Bedfordsire, MK43 0AL, UK

Keywords: Metal foam heat exchanger, heat transfer, pressure drop, multi-objective optimization, Micro gas turbine.

Abstract

Small size and high efficiency of micro gas turbines require a higher surface-to-volume ratio of recuperators. Conventional recuperators can achieve a range of 250-3600 m^2/m^3. Advances in materials and manufacturing, such as metal foams, can increase significantly the exchange surface and improve compactness ranging approximately from 500 to over 10,000 m^2/m^3, due to their exceptional micro geometry. The main advantage is that the increase of surface area does not impact the cost of the heat exchanger as much as conventional recuperators due to their easy manufacturing. This work addresses the optimisation of the recuperator using multiple objectives satisfying efficiency, power output and weight criteria, offering a holistic approach that takes into account the entire system rather than individual components or channels. A model is developed to represent the performance of a compact heat exchanger in micro gas turbines. The recuperator is an annular heat exchanger with involute profile filled with porous media in a counterflow arrangement on the hot and cold sides. The model allows the evaluation of the effect of the recuperator geometry features on the electrical efficiency, power output and weight savings in a micro gas turbine. Existing models for the global heat transfer coefficient, effective thermal conductivity, surface area and pressure drop of porous media are selected and implemented. The design variables of multi-objective are the pore density, porosity and number of channels, whilst the objectives are the overall electrical efficiency, power output and recuperator weight. The problem is solved using the Non-Dominated Sorting Genetic Algorithm (NSGA-II) to determine an approximation of the Pareto front, whilst the accuracy of the approximation is assessed against the solution obtained by an exhaustive search. The comparison shows that NSGA-II outperforms an exhaustive search by at least 90% in terms of computational efficiency. These results allow the quantification of the impact of metal foam technology on performance metrics of the recuperator as well as the entire system. This quantitative analysis provides valuable insights into the behaviour of metal foam recuperators in μ-GTs. An optimal design with 30% efficiency and 28 kW power output appears in pore densities of approximately 10 and 20 pores per inch (PPI) for the air and gas side respectively, and a porosity of 85%, which leads to a state-of-the-art recuperator weight of 48 kg. The efficiency improvement over the industry standard is 15%, with only a 2.5% reduction in power output.

Published by Elsevier. This is the Author Accepted Manuscript issued with: Creative Commons Attribution License (CC:BY 4.0).
The final published version (version of record) is available online at DOI:10.1016/j.applthermaleng.2024.122410. Please refer to any applicable publisher terms of use.

Nomenclature

A_c	cross sectional area (m^2)
A_{exc}	exchange area (m^2)
a_{sf}	surface area density (m^{-1})
Bi	Biot number (-)
C	heat capacity rate (W/K)
Cr	ratio of the two heat capacity rates (-)
c_p	specific heat capacity (J/kg K)
d_f	ligament diameter (m)
d_p	pore diameter (m)
e	dimensionless cubic node length (-)
F	inertial coefficient (-)
f	dimensionless friction factor (-)
H	channel foam thickness (m)
h	heat transfer coefficient (W/m^2K)
j	Colburn factor (-)
K	permeability (m^2)
k	thermal conductivity (W/m K)
L	length (m)
$\dot{m}$	mass flow rate (kg/s)
n_c	number of channels (-)
Nu_H	channel Nusselt number (-)
p	pressure (Pa)
Pr	Prandtl number (-)
pr	pressure ratio
$\dot{Q}$	heat rate (W)
R	radius (m)
Re_d	Reynolds number for pore ligament (-)
Re_H	Reynolds number for channel (-)
S	involute curve channel length (m)
T	temperature (K)
t	wall thickness (m)
U	overall heat transfer coefficient (W/m^2K)
u	velocity (m/s)
$\dot{W}$	power (W)
W_R	recuperator weight (kg)
α	pressure angle of involute geometry (rad)
ε	effectiveness (-)
η	efficiency (-)
κ	ratio of effective thermal conductivities (-)
λ	dimensionless foam ligament radius (-)
μ	viscosity (kg/s m)
ρ	density (kg/m^3)
φ	porosity (-)

Subscripts

c	Channel
e	Effective
el	Electrical
is	Isentropic

f	Fluid
i	Internal
o	Outer
R	Recuperator
s	Solid
sf	Interstitial

Acronyms

CAD	Computer Aided Design
CFD	Computational Fluid Dynamics
DLS	Direct Laser Sintering
GA	Genetic Algorithm
GD	Generational Distance
LMTD	Logarithmic Mean Temperature Difference
NSGA-II	Nondominated Sorting Genetic Algorithm
NTU	Number of Transfer Unit
PCM	Phase Changing Material
PEC	Performance Evaluation Criteria
PF	Pareto Front
PPI	Pores per Inch (pore density)
PSHE	Primary Surface Heat Exchanger
SLM	Selective Laser Melting
TPF	Theoretical Pareto Front
μ-GT	Micro gas turbine

1. Introduction

Compact heat exchangers are becoming increasingly popular in aerospace, automotive, and power generation industries motivated by the need for decentralised power generation and energy savings [1]. Micro gas turbines (μ-GTs), which generate power of about 500 kW or below, are an attractive solution for this market [2]. These turbines have lower CO and NO_x emissions, but their typical efficiency range is 15-20% when the efficiency of larger scale turbines ranges from 35 to 40%. Thermal management can be used to increase the efficiency of μ-GT using intercoolers, cooling-air coolers or recuperators [3]. Heat exchangers are used as recuperators in gas turbines to recover waste heat from the exhaust gas and transfer it to the incoming air, to improve overall efficiency. Externally fired configurations of μ-GTs can achieve an efficiency of 30% without increasing recuperator cost [4]. To satisfy cost constraints, it is necessary to maintain simplicity in the system design and ensure compact packaging [5]. However, recuperators add weight and complexity to the system, accounting for 25-30% of the overall cost of μ-GT [6]. Recuperator weight or material volume can be considered a cost metric for μ-GT applications; however, the cost depends on the specific application and the priorities of the system designer [6, 7]. In some μ-GT applications, such as mobile or portable systems, weight and size may be a critical factor. In these cases, designers need to balance the benefits of improved efficiency with the added weight and cost.

Metal foams are a highly desirable class of materials for lightweight structures and heat transfer applications, primarily due to their high surface area per unit volume. The integration of metal foam into heat exchangers generally enhances overall performance when compared to hollow channels [8, 9]. One of the key benefits of incorporating metal foam into channels compared to conventional Primary Surface Heat Exchangers (PSHE) is the ability to manipulate process

parameters to create metal foams with different levels of porosity and pore densities. In contrast, PSHEs require extensive development to establish the process parameters for manufacturing [10]. Printed circuit heat exchangers have been introduced in the market for use as recuperators due to the low capital cost compared to a conventional heat exchanger. However, they are relatively heavy due to the low porosity [1].

The thermal and fluid dynamics performance is critical for the evaluation of performance from a single channel level to a heat exchanger. Effectiveness, heat transfer, Colburn factor j, pressure drop, and the dimensionless friction factor f can be used as metrics for these characteristics in relation to pore size and porosity [11, 12, 13, 14]. Numerous pressure drop correlations have been put forward to analyse the flow dynamics in metal foams. One commonly employed method treats the internal flow in metal foam as analogous to pipe flow [15]. In this approach, the pressure drop is estimated by utilising the friction factor [16, 17]. Other pressure drop models are based on the Ergun equation [18, 19], which relates the pressure drop to the flow velocity and properties of the porous medium. This model represents the viscous and inertial resistance caused by fluid flow through the porous structure. The main objective for high thermo-fluid performance is to maximise the j/f ratio of the metal foam with optimal porosity ranging between 0.85 and 0.95 [20]. Findings in a parallel-plate channel with metal foam suggest optimal performance at maximised $j/f^{1/3}$, at the same porosity range and a pore density between 10 PPI and 20 PPI [21]. Several experimental and analytical studies have been conducted to evaluate the performance of metal foams in various configurations, such as aluminium alloy in a plate-foam heat exchanger [22, 23, 24], and metal foam inside a tube [25] or in the annular channel of tube-in-tube configurations [26]. Metal foams offer higher heat transfer performance than longitudinal and spiral fins with the same surface density [24]. A shell and tube configuration built by wrapping metal foam around the outside of a metal tube has achieved up to 71% heat transfer enhancement [27]. The presence of metal foam both inside and outside the tube is necessary for improved overall performance due to the inefficient heat transfer between the internal mass stream in an empty tube and the wall. Numerical investigations have explored the performance of a metal foam baffle cut shell and tube heat exchanger and demonstrated that it is an optimal choice compared with conventional metal baffle heat exchangers [28]. For the same efficiency and fan power, metal foam heat exchangers are smaller in size and lighter than finned configurations [29]. However, despite their potential in enhancing heat transfer performance and reducing the size and weight, the adoption of metal foams as a cost-effective manufacturing technology for porous media heat exchangers is still in the early stages of development. Nonetheless, significant progress is being made, with the advancements including the utilisation of dissolution and powder sintering techniques [30], additive manufacturing, like 3D printing and Selective Laser Melting (SLM) [31, 32], as well as Direct Laser Sintering (DLS) [33, 34] allowing flexibility in material selection and design complexity for lightweight structures.

The primary aim of recuperator design is to determine an optimal geometry that balances various factors and requirements such as heat transfer effectiveness, pressure drop, compact size, and cost. The trade-off between maximising heat transfer and minimising pressure drop is a common challenge in heat performance and fluid flow analysis. Enhancing heat transfer often leads to increased pressure drop, resulting in conflicting objectives. Achieving an appropriate balance between these parameters is crucial for each application. Numerous studies have approached this matter directly by considering heat transfer and pressure drop as objective functions [35]. Multi-objective optimisation has been applied to porous media by using dimensionless functions such as the Nusselt number or Performance Evaluation Criteria (PEC) for more generic outcomes

[36, 37, 38, 39]. Zheng et al. [40] employed a Genetic Algorithm coupled with Computational Fluid Dynamics (CFD), to optimise heat transfer under constant pumping power in a uniformly heated tube by finding optimum porosity distributions along the radial direction in a single and in multiple layers. Multiple layers increase PEC to values 2.5 times higher than a single layer whilst the optimal porosity is above 95%. Du et al. [41] coupled CFD with a Genetic Algorithm (GA) optimising flow resistance and thermal efficiency in a volumetric solar receiver equipped with a ceramic foam. GAs have also been used to optimise the porosity distribution of metal foams in solar receivers maximising radiative heat transfer [42]. A multi-objective Genetic Algorithm (NSGA-II) has been applied to optimise metal foam heat sinks, taking into account various geometrical, and fluid-dynamic design variables to minimise material cost and operational time of phase changing materials [43]. This approach has also been employed to address the trade-off between heat transfer and pumping power in metal foam heat sinks modifying design variables for finned and non-finned cases [44].

Microturbine coupled foam recuperators are not yet fully explored as a solution. This technology combines the advantages of porous media properties for heat transfer enhancement, compactness, and low weight. However, the complexity of variable interactions renders porous recuperator performance hard to predict. A high-performance metal or ceramic foam recuperator integrated in a μ-GT has not been introduced yet, due to the costly and complex manufacturing. Therefore, experimental results from such a solution are not available. Currently, there are no studies in the literature that predict the performance of μ-GT equipped with a porous media recuperator. Analytical and experimental models address simple designs of a low number of rectangular or cylindrical channels. The computations cost of full-scale numerical analysis of a porous media is prohibitive. As a result, existing research considers either empirical correlations for porous zone domains or a small channel with reconstructed metal foam. Reconstruction of a three-dimensional Computer-Aided Design (CAD) geometry foam is challenging in terms of an exact representation. There is not enough knowledge on the effects of foam incorporation to the overall performance of μ-GT. Xiao et al [45] suggested a framework that instead of focusing on the recuperator, it interconnects the recuperator characteristics with the μ-GT system and optimisation algorithms, offering a holistic approach.

This study develops, implements and applies a methodology for identifying the optimal combination of design variables that maximise electrical efficiency and power output whilst achieving weight minimisation in μ-GTs using metal foam recuperators. The approach involves a combination of heat transfer and pressure drop correlations at a single channel level. This study implements the framework proposed by Xiao et al. [45] to establish how variations of metal foam recuperator design parameters influence electrical efficiency, weight, and the power output of μ-GTs and use this to optimise the overall design. While previous studies have explored the performance at the level of a single channel, this work investigates the integration of metal foam heat exchangers into μ-GTs and the impact of porous geometry on recuperator weight, heat transfer and pressure losses as well as on system efficiency and power output. Pareto multi-objective optimisation is conducted by running a GA within established design constraints and results are compared with a current primary surface heat exchanger available in the market. By considering the whole μ-GT rather than just a single channel or component, a better understanding can be gained of how the system operates in its entirety and how it can be improved.

2. Methodology

The development steps in this work comprise a) calculation of annular flow with involute profile channels to analyse the involute geometry; b) performance modelling of foam recuperator; c) comparison of heat transfer and pressure drop correlations in a metal foam filled channel for valid model selection; d) thermodynamic analysis of recuperated cycle; and e) multi-objective optimisation using NSGA-II. The methodology is implemented in Python 3.8. To enable a comprehensive comparison, the present recuperator is evaluated against the Capstone C30 μ-GT system, which serves as an established industry reference. To ensure an accurate and meaningful comparison, the recuperator external dimensions, including the recuperator length, internal and external diameter, as well as thermodynamic specifications, have been fixed to match those of C30 [46, 47].

2.1. Annular flow configuration of metal foam recuperator with involute profile channels

The problem under consideration corresponds to forced convective steady state heat transfer with hot and cold streams through porous media channels. The design of air and gas streams in the recuperator uses an involute profile as shown in Figure 1 (a), which allows a tight arrangement of the channels in the annular space. The involute curve length S is defined by its representation in polar coordinates:

$$cos\,\alpha = R_i/R_o\ , \qquad S = R_i\,(tan\,\alpha)^2/2 \tag{1}$$

where R_i and R_o are the base and outer circle radii respectively, and α is the pressure angle between the radius vector and line tangent to the involute as shown in Figure 1 (b). The opening distance H of a channel on a plane normal to S and to the flow is calculated as:

$$H = 2\pi R_i/n_c \tag{2}$$

where n_c is the total number of channels. Therefore, the cross-sectional area normal to flow direction at each channel is:

$$A_c = H\,S + \left(\frac{\pi(R_o^2 - R_i^2) - H\,S\,n_c}{n_c}\right) \tag{3}$$

The flow velocity of each fluid represents the Darcy velocity of the channel:

$$u_c = \frac{\dot{m}_c}{\rho_f A_c} \tag{4}$$

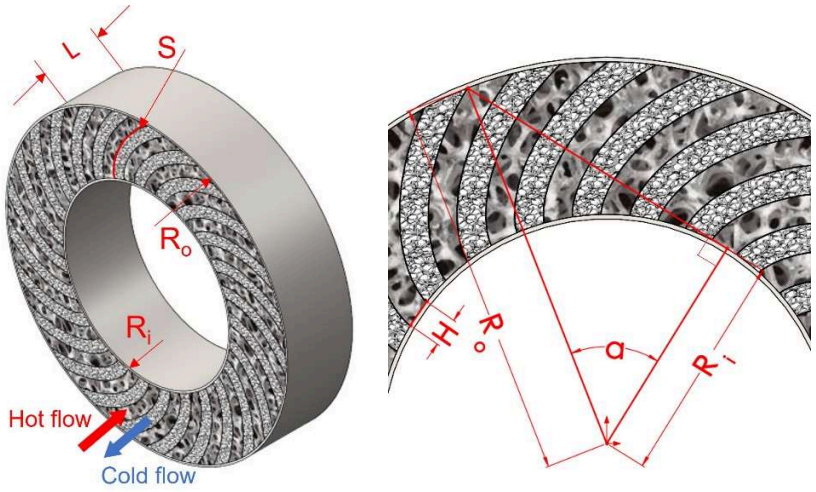
where ρ_f is the density of the fluid. Here $\dot{m}_c$ is the mass flow rate at each channel which is obtained by dividing the total mass flow rate of each working fluid by half of the number of channels. The channel Reynolds number is obtained by the flow velocity of each channel and the characteristic length, which is $2H$, as follows:

$$Re_H = \rho_f u_c 2H/\mu \tag{5}$$

where μ is the fluid dynamic viscosity. The total weight of the recuperator can be determined using:

$$W_R = 1.5\rho_s L\left(\left(\pi R_o^2 - \pi R_i^2\right)(1-\varphi) + tSn_C\right) \tag{6}$$

where t is the wall thickness which separates the cold with the hot channels and ρ_s is the density of solid material. A correction coefficient of 1.5 has been proposed to account for the weight of auxiliary parts [46]. This is used in the present study. The number of channels, n_c, and metal foam porosity, φ, are two of the four design variables used in the optimisation.



(a) (b)

Figure 1: a) A 3D model of recuperator with involute profile channels filled with metal foam in hot and cold sides. b) a detail view with geometry characteristics of involute profile.

2.2. Thermal and pressure drop modelling of foam filled recuperator

The metal foam heat exchanger is modelled with annular involute profile channels in a counter flow configuration. The heat transfer rate in the heat exchanger is defined considering that there is no mixing and crossflow [46]:

$$\dot{Q}_R = UA_{exc}LMTD \tag{7}$$

where LMTD is the Logarithmic Mean Temperature Difference:

$$LMTD = \frac{\left(T_{gas,in} - T_{air,out}\right) - \left(T_{gas,out} - T_{air,in}\right)}{ln\left[\frac{\left(T_{gas,in} - T_{air,out}\right)}{\left(T_{gas,out} - T_{air,in}\right)}\right]} \tag{8}$$

Temperatures $T_{gas,in}$ and $T_{air,in}$ refer to inlet temperatures, and $T_{gas,out}$ and $T_{air,out}$, to outlet temperatures for gas and air respectively. The necessary heat exchange area refers to the wall between the channels as this is the direct exchange area [26]:

$$A_{exc} = L\, S\, n_c \tag{9}$$

The effectiveness of a heat exchanger (ε) is defined as the ratio of the actual heat transfer rate to the maximum possible heat transfer rate and expressed as: $\varepsilon = \dot{Q}\ /\dot{Q}_{max}$ or for a counterflow as

$$\varepsilon = \frac{1 - e^{-NTU(1+C_r)}}{1 - C_r e^{-NTU(1+C_r)}} \tag{10}$$

with NTU the number of transfer units defined as:

$$NTU = UA_{exc}/C_{min} \tag{11}$$

and

$$C_r = \frac{C_{min}}{C_{max}},\ C_{min} = min\left(\dot{m}_{air}Cp_{air},\ \dot{m}_{gas}Cp_{gas}\right),\ \ C_{max} = max\left(\dot{m}_{air}Cp_{air},\ \dot{m}_{gas}Cp_{gas}\right) \tag{12}$$

where C_{min} and C_{max} are the minimum and maximum heat capacity rates between the hot and cold stream respectively. Heat capacity rate is computed as the product of the total mass flow rate ($\dot{m}_{gas}$ and $\dot{m}_{air}$ for gas and air respectively), and the specific heat capacity (Cp_{gas} and Cp_{air}). The energy balance between the hot and cold streams dictates the total heat transfer rate in the heat exchanger as follows:

$$\dot{Q} = \dot{m}_{air}Cp_{air}\left(T_{air,out} - T_{air,in}\right) = \dot{m}_{gas}Cp_{gas}\left(T_{gas,in} - T_{gas,out}\right) \tag{13}$$

Assuming negligible variations of thermophysical properties, the model uses the average temperature of the working medium at the recuperator inlet and outlet for the design process. The thermophysical properties required for the process are obtained using an open-source thermophysical property library (CoolProp) [48]. The stainless steel that is used in the current heat exchanger has lower thermal conductivity (16.3 [W/mK]) than the bonding material of [49], supporting the assumption of negligible contact thermal resistance between the porous media material and channel walls. Negligible fouling resistance is also assumed. In addition, the recuperator has a thin wall thickness, allowing the wall thermal resistance to be neglected. The overall heat transfer coefficient U of the recuperator is:

$$\frac{1}{U} = \frac{1}{h_{air}} + \frac{1}{h_{gas}} \tag{14}$$

where h_{air} and h_{gas} are the convective heat transfer coefficients of the cold and hot stream respectively. Numerical correlations are used to calculate the heat transfer coefficients and pressure drop in the recuperator. The air and gas side heat transfer coefficient h is:

$$h = \frac{Nu_H k_f}{2H} \tag{15}$$

where k_f is the fluid thermal conductivity. The channel Nusselt Nu_H number is calculated according to [50]:

$$Nu_H = 12\frac{1+\kappa}{\kappa}\frac{1}{1 + \frac{3}{Bi(1+\kappa)}\left[1 - \frac{1}{\sqrt{\frac{Bi(1+\kappa)}{\kappa}}}tanh\left(\sqrt{\frac{Bi(1+\kappa)}{\kappa}}\right)\right]} \tag{16}$$

where Bi serves as an equivalent Biot number, corresponding to the ratio of conduction resistance within the solid phase to the thermal resistance associated with the internal convective heat exchange between the solid and fluid phases. Parameter κ denotes the ratio of effective thermal conductivities between the fluid and solid phases.

$$Bi = h_{sf}a_{sf}\,H^2/k_{se}\,,\qquad \kappa = k_{fe}/k_{se} \tag{17}$$

To estimate the interstitial heat-transfer coefficient, the empirical model developed by Zukauskas for orthogonally stacked cylinders [51] is utilised:

$$Nu_{sf} = \frac{h_{sf} d_p}{k_f} = \begin{cases} 0.76 Re_d^{0.4} Pr^{0.37}, & 1 \le Re_d \le 40 \\ 0.52 Re_d^{0.5} Pr^{0.37}, & 40 \le Re_d \le 10^3 \\ 0.26 Re_d^{0.6} Pr^{0.37}, & 10^3 \le Re_d \le 2 \times 10^5 \end{cases} \quad (18)$$

The estimation of Reynolds number Re_d is based on pore ligament diameter d_f as follows:

$$Re_d = \rho_f u d_f / \mu \quad (19)$$

The interstitial velocity, u, is calculated by dividing the superficial velocity by the open pore area fraction. Porous media properties, such as surface area density a_{sf} and ligament diameter d_f, are calculated from porosity φ and pore diameter d_p [52]:

$$d_p = 0.0254/PPI \quad (20)$$

$$\frac{d_f}{d_p} = 1.18 \cdot \sqrt{\frac{(1-\varphi)}{3 \cdot \pi}} \cdot \left(\frac{1}{1 - e^{-\left(\frac{1-\varphi}{0.04}\right)}} \right) \quad (21)$$

$$a_{sf} = \frac{3 \cdot \pi \cdot d_f \cdot 1 - e^{-\left(\frac{1-\varphi}{0.04}\right)}}{\left(0.59 \cdot d_p\right)^2} \quad (22)$$

The effective foam thermal conductivity is determined based on the three-dimensional tetradecahedron structure as proposed by Boomsma and Poulikakos [53]:

$$k_e = \frac{\sqrt{2}}{2(R_A + R_B + R_C + R_D)} \quad (23)$$

where:

$$R_A = \frac{4\lambda}{\left(2e^2 + \pi\lambda(1-e)\right)k_s + \left(4 - 2e^2 - \pi\lambda(1-e)\right)k_f} \quad (24)$$

$$R_B = \frac{(e-2\lambda)^2}{(e-2\lambda)e^2 k_s + (2e - 4\lambda - (e-2\lambda)e^2)k_f} \quad (25)$$

$$R_C = \frac{\left(\sqrt{2} - 2e\right)^2}{\left(2e^2 + \pi\lambda(1-e)\right)k_s + \left(4 - 2e^2 - \pi\lambda(1-e)\right)k_f} \quad (26)$$

$$R_D = \frac{2e}{e^2 k_s + (4 - e^2)k_f} \quad (27)$$

introducing the dimensionless foam ligament radius λ and using a value of 0.339 for the dimensionless cubic node length e as the best agreement with experimental data [53]:

$$\lambda = \sqrt{\frac{\sqrt{2}(2 - \left(\frac{5}{8}\right)e^3\sqrt{2} - 2\varphi}{\pi\left(3 - 4e\sqrt{2} - e\right)}} \quad (28)$$

The effective solid thermal conductivity k_{se} is defined by setting $k_f = 0$. Similarly, the effective fluid conductivity k_{fe} is established by setting $k_s = 0$.

Permeability K and inertial coefficient F correlations are the primary models used to predict the pressure drop in homogeneous and isotropic porous media, based on Forchheimer's extended Darcy's equation:

$$\frac{dp}{dx} = \frac{\mu_f}{K}u + \frac{\rho_f F}{\sqrt{K}}u^2 \tag{29}$$

The model suggested by Calmidi [52] for the determination of the two coefficients in Eq. (29) is used to calculate the permeability K and inertial coefficient F as follows:

$$K = 0.00073(1-\varphi)^{-0.224}\left(\frac{d_f}{d_p}\right)^{-1.11} {d_p}^2 \tag{30}$$

$$F = 0.00212(1-\varphi)^{-0.132}\left(\frac{d_f}{d_p}\right)^{-1.63} \tag{31}$$

2.3. Heat transfer and pressure drop correlations in a parallel plate channel

Figure 2 illustrates a comparison of heat transfer correlations in a parallel plate channel. It is assumed that the flow is fully developed both thermally and in terms of fluid dynamics, thermodynamic properties of the solid and fluid are not affected by temperature variations, and natural convection and radiation are negligible. The porous medium is also assumed to be homogeneous and isotropic. The comparison is conducted on a single rectangular channel with air flow through open cell metal foam of 10 PPI and 93% porosity at a valid Reynolds number range as well as a geometrical aspect ratio, L/H, of 4. The selected material is Al. The model developed by Lee-Vafai [50] is based on the analytical solution of dimensionless fluid temperature by solving the coupled energy balance equations accounting for transverse conduction contributions and constant wall heat flux boundary conditions in a channel. This model is chosen for the calculation of heat transfer in the recuperator within the thermodynamic cycle under investigation as it offers great flexibility as it can be applied to different foam and working media materials, pore densities, and porosities. Thus, it can be used in parametric design and optimisation studies of foam heat exchangers. Besides, the comparison of heat transfer models shows that this model is within the intermediate values between 32 and 80. Apart from one study that overestimates heat transfer [12], the heat transfer models show good agreement, with a maximum error band of less than 26%. This error band is considered acceptable, as it falls within the typical range of uncertainties associated with heat transfer correlations. The selected model within this error range ensures suitability for this study, providing confidence in its application to different pore densities, and porosities. The channel Nu number, Nu_H, used here is the average Nu number, which apply to the critical length of the channel rather than the pore. For example, studies [12, 13, 14] use a fin efficiency and an effective fin length to calculate the channel heat transfer coefficient and channel Nu number. This Nu number, Nu_H, is influenced by the interstitial Nu number, Nu_{sf}, which is based on the ligament diameter length scale. The different models of channel Nu number have a similar increase with Re number as fluid mixing is enhanced.

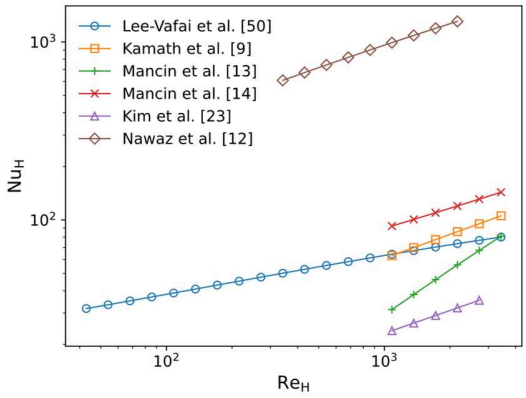


Figure 2: Comparison of heat transfer correlations referring to channel Nu number as a function of channel Re number.

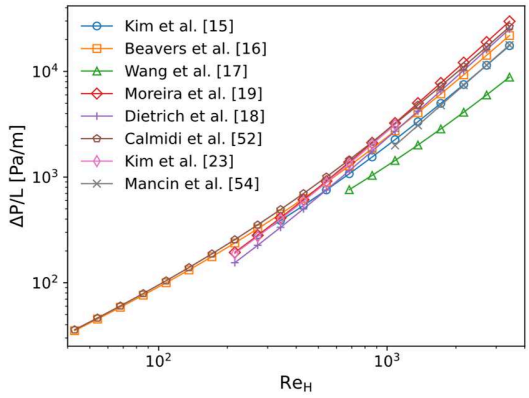


Figure 3: Comparison of pressure drop correlations referring to pressure loss in a channel as a function of channel Re number.

The different pressure drop correlations inside a metal foam filled channel are compared in Figure 3. The pressure losses calculations from [15, 16, 17, 23, 54] are based on a friction factor as a function of experimental permeability. The other three models [18, 19, 52] estimate pressure losses according to the Darcy-Forchheimer equation. The model proposed by Calmidi et al [52] was chosen for the calculation of pressure losses in the recuperator of the present study. This choice is based on correlations developed also by Calmidi et al [52] for pore diameter, surface area density, permeability, and inertia coefficient, all of which are utilised in the present study. Furthermore, this model has the second highest values of pressure drop at high Re numbers after [19], placing it among the most conservative choices. Various studies report substantial variations in the dimensionless friction factor associated with pressure drop correlations [9, 55]. The maximum error band in this comparison at high Reynolds numbers is 36%. However, among the models considered, the majority exhibit small maximum error bands of 3% and 22% at low and high Re numbers, respectively. Wang's model [17] underestimates pressure drop within the measured range, while Dietrich's model [18] underestimates it at Re numbers between 217 and 800.

2.4. Model of recuperated cycle

The potential of integrating a metal foam filled recuperator in a μ-GT is investigated utilising Python 3.8 in a Brayton cycle simulation. The thermodynamic model comprises two main components: (i) the calculation of the thermodynamic properties of the Brayton cycle components using ideal gas thermodynamics and (ii) the use of a recuperator model. The first part defines the inputs of the simulation including initial conditions and design parameters. The cycle and geometrical recuperator specifications considered in this analysis, are listed in Table 1. These specifications are chosen to match C30 data [46, 47] within the typical operating range, to facilitate a fair performance comparison with the optimised design points. The thermodynamic cycle commences with the air flow entering the compressor. Upon exiting the compressor, the air obtains a higher pressure and a polytropic efficiency of 0.8. The exhaust gases then expand in the turbine, where they undergo an expansion with an isentropic efficiency of 0.84. During the first cycle, values are calculated at each state of compressor, combustor and turbine. The combustion process is modelled by assuming a constant pressure heating process in which fuel is added to

compressed air. Fuel and air are modelled using a library for simulation of chemical kinetics [56], and the mass flow rate of each component is calculated based on a given equivalence ratio of the mixture. The temperature at the turbine inlet is calculated based on the heat added to the system. The state variables of the thermodynamic states, including their respective enthalpies, are determined based on the simplified schematic diagram presented in Figure 4(a). The electrical efficiency is computed using:

$$\eta_{el} = \frac{\dot{m}_{gas}\ c_{p\,gas}(T_3 - T_4) - \dot{m}_{air}\ c_{p\,air}(T_2 - T_1)}{(\dot{m}_{gas}\ c_{p\,gas}\ T_3 - \dot{m}_{air}\ c_{p\,air} T_2)} \tag{32}$$

In this configuration the efficiency is computed as the difference between the turbine work ($\dot{m}_{gas}\ c_{p\,gas}\ (T_3 - T_4)$) and the work consumed by the compressor ($\dot{m}_{air}\ c_{p\,air}\ (T_2 - T_1)$), divided by the heat input from the combustor ($\dot{m}_{gas} c_{p\,gas} T_3 - \dot{m}_{air}\ c_{p\,air}\ T_2$). Temperatures T_2 and T_4 are identical to $T_{air,in}$ and $T_{gas,in}$ from Eq. (8), respectively.

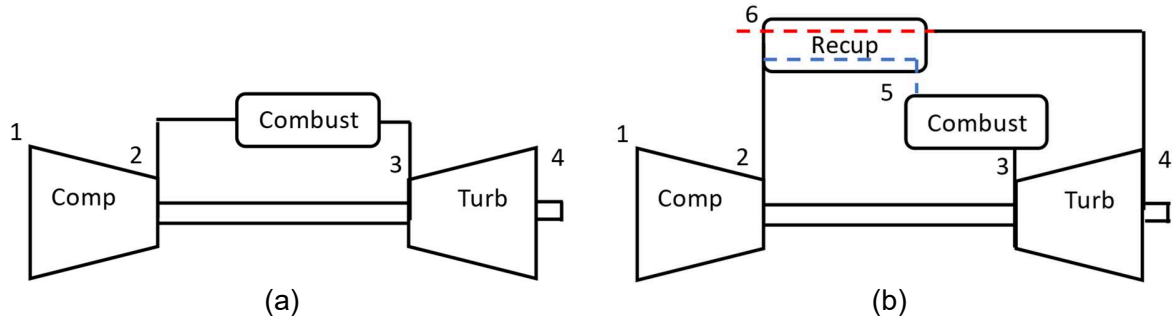


Figure 4: Schematic of thermodynamic Brayton cycle gas turbine (a) without recuperator and (b) with recuperator.

The next part of the code calls the recuperator model, which takes as inputs the mass flow rate of air, mass flow rate of fuel, inlet temperature of hot stream, inlet temperature of the cold stream, and inlet and outlet pressures of both streams. The model calculates outlet temperatures, the pressure drop in both streams and the recuperator heat transfer rate. Compressed air is directed through the recuperator as shown in the schematic in Figure 4(b). The heat exchanger heats the compressed air from state 2 to state 5 through the transfer of heat from the exhaust gases that exit the turbine at state 4 following Eq. (7). The exhaust gas exits the system at a lower temperature, T_6. As a result, the heated air enters the combustion chamber, where it ignites upon mixing with the incoming fuel. In this case, in the efficiency definition, the power output is divided by the difference between the heat input and the heat recovered by the exhaust ($\dot{m}_{gas}\ T_5 - \dot{m}_{air}\ T_2$). Temperature T_5 is identical to $T_{air,out}$ of Eq. (7).

The model also takes into account the impact of recuperator pressure drop on power output and efficiency. The compressed air has a slightly lower pressure p_5 at the entrance of the combustor than p_2 at the exit of compressor, due to the pressure losses Δp_{air} that occur in the recuperator as calculated by Eq. (29). Additionally, in the turbine, there is a work fraction that is exploited by the heat exchanger due to expansion at a higher pressure p_{4new} where pressure losses at the gas side Δp_{gas} are added to pressure at the exit of turbine p_4. The new pressures are calculated as follows:

$$p_5 = p_2 - \Delta p_{air} \tag{33}$$

$$p_{4new} = p_4 + \Delta p_{gas} \tag{34}$$

The turbine in this case expands the fluid at a temperature T_{4new} that is calculated based on the new pressure p_{4new}.

Table 1: Specifications of the recuperated Brayton cycle considered.

Property	Value
Compressor inlet temperature $\boldsymbol{T_1}$ (K) (15 °C ISO conditions)	288.15
Air mass flow rate $\dot{\boldsymbol{m}}_{\boldsymbol{air}}$ (kg/s)	0.308 [47]
Fuel mass flow rate $\dot{\mathbf{m}}_{\mathbf{fuel}}$ (kg/s)	0.0023 [47]
Gas mass flow rate $\dot{\boldsymbol{m}}_{\boldsymbol{gas}}$ (kg/s)	0.31 [47]
Pressure ratio $\boldsymbol{pr}$	3.64 [47]
Turbine isentropic efficiency $\boldsymbol{\eta_{isT}}$	0.84 [47]
Compressor polytropic efficiency $\boldsymbol{\eta_{isC}}$	0.8 [47]
Recuperator core internal radius $\boldsymbol{R_i}$ (m)	0.1265 [46]
Recuperator core external radius $\boldsymbol{R_o}$ (m)	0.2175 [46]
Recuperator core length $\boldsymbol{L}$(m)	0.2 [46]
Wall thickness $\boldsymbol{t}$ (m)	0.0001 [46]
Material	Stainless Steel Alloy 347 [46]

2.5. Multi-objective optimisation of involute profile metal foam recuperator

The multi-objective optimisation problem of designing a counter-flow heat exchanger with metal foam, is solved using pymoo [57], a Genetic Algorithm toolbox in Python 3.8. The optimisation process uses the NSGA-II [58] algorithm to solve the problem which evolves a population of candidate solutions, with each individual in the population representing a possible solution to the problem. To start the calculation, an initial population of solutions is established and fed into a thermodynamic μ-GT model. The model calculates the output for each individual. The algorithm then assesses the outputs and selects a new set of individuals representing design solutions using non-dominated sorting and crowding distance sorting to select the best solutions from the population, ensuring diversity and a good spread of solutions in the objective space. The objectives of the optimisation are to maximise electrical efficiency and power output and to minimise recuperator weight. For maximisation objectives, the problem is redefined by minimising their negative values. A flowchart of the overall algorithm is presented in Figure 5. The design variables for the current problem include both the geometry of the metal foam and the number of channels. In particular, the number of channels is an integer variable that is defined as part of a mixed variable problem. Selected parameters are the foam pore density on the air and gas side and the porosity. While the dimensions of the heat exchanger depend on angle α or involute length S, the selected design variables do not affect these dimensions. This design choice enables a meaningful comparison with industry standards with the same dimensions. Here, the design variables vector $\boldsymbol{x} \in \mathbb{R}^3 \times \mathbb{N}$ is $\boldsymbol{x} = [PPI_{air},\ PPI_{gas},\ \varphi,\ n_c]$ with the design parameter ranges reported in Table 2 . The multi-objective optimisation problem is formulated as follows:

$$\begin{gathered} \{PPI_{air}, PPI_{gas}, \varphi, n_c\} = \\ argmin\left(-\eta_{el}(PPI_{air}, PPI_{gas}, \varphi, n_c), -\dot{W}_{el}(PPI_{air}, PPI_{gas}, \varphi, n_c), W_R(PPI_{air}, PPI_{gas}, \varphi, n_c)\right) \\ subject\ to \begin{matrix} T_5 \leq 1100 \\ H > 1.2 d_p \end{matrix} \end{gathered} \tag{35}$$

Table 2 Design parameter ranges.

Parameters	Ranges
Air pore density $\boldsymbol{PPI_{air}}$	8-40
Gas pore density $\boldsymbol{PPI_{gas}}$	8-40
Porosity $\boldsymbol{\varphi}$	0.85-0.97
Number of channels $\boldsymbol{n_c}$	100-260

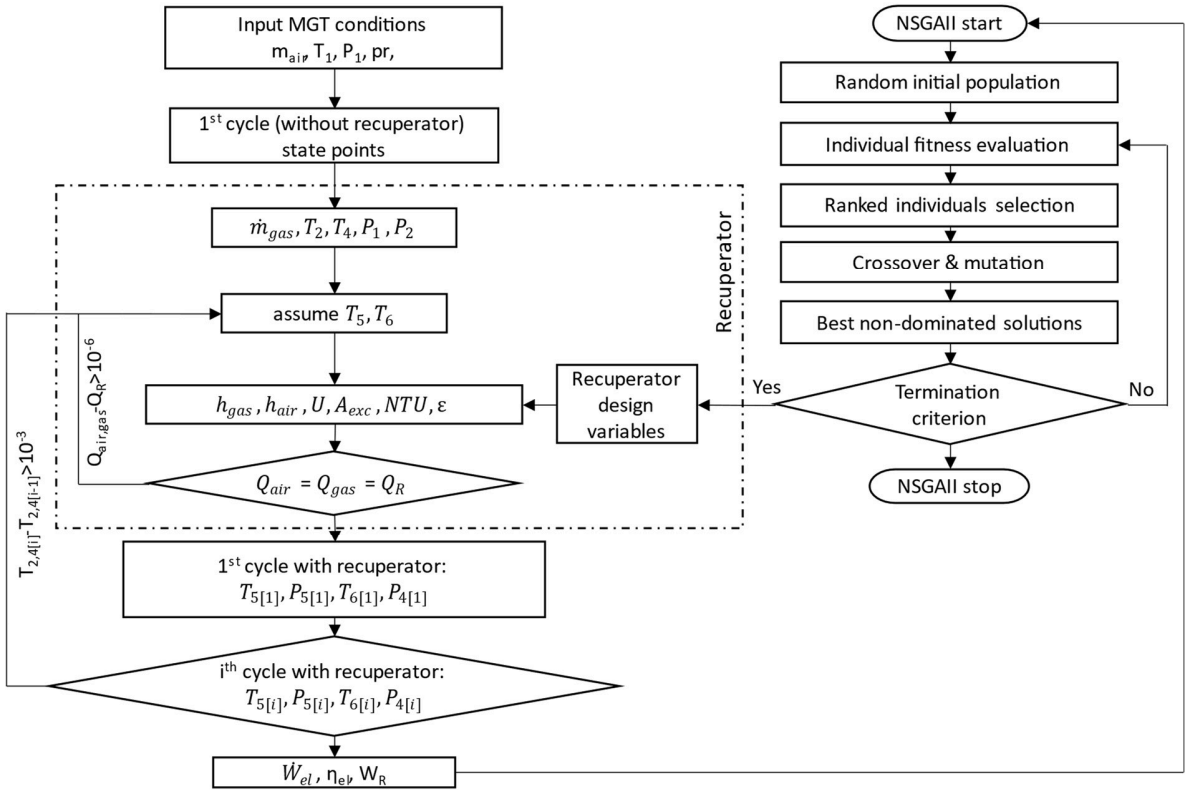


Figure 5: Methodology flowchart of optimisation of recuperated Brayton cycle performance using NSGA-II.

Genetic Algorithms need reliability testing to assess the reproducibility of problem solutions and their convergence characteristics [59]. To evaluate the effectiveness of the GA for this problem and demonstrate its convergence within a reasonable number of generations, a metric needs to be established. This metric measures the distance between the Pareto front at each generation and either the last generation Pareto front or a theoretical Pareto front. The theoretical Pareto front is determined here through an exhaustive search involving 200,000 and 300,000 points, using a simple Pareto dominance-based sorting algorithm. This algorithm iteratively compares each point with others to establish dominance relationships. The distance calculation is based on the coordinates of the individuals in both fronts, using the Euclidean distance. This process is repeated for all individuals, and the average of the minimum distances are used to indicate generational distance (GD) between the two fronts. NSGA-II has been evaluated using different parameters as presented in Table 3 to assess reliability, robustness, and reproducibility. The GA needs 32,000 evaluations to complete the analysis, considering populations size of 80 and 400 generations which was set as termination criterion. Among these evaluations, approximately 30,000 points were found to satisfy the given constraints. The tests include changes in cross over

probability, mutation probability for real and integer variables to assess its impact on the algorithm performance and mutation eta that influences the intensity of mutations applied during the evolutionary process.

Table 3 GA parameters for optimisation

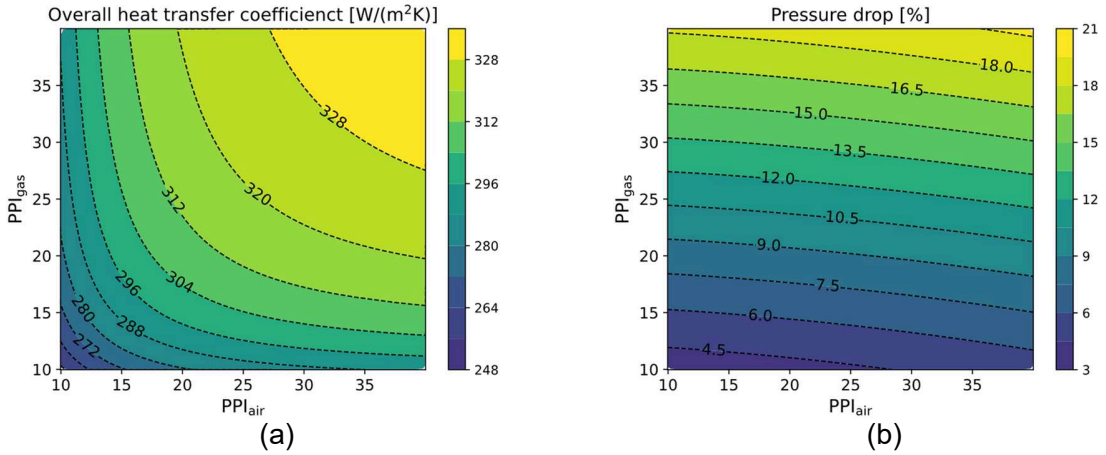
	NSGA-II adjustments					
Run	Generations	Population size	Crossover prob	mutation prob real	mutation prob integer	mutation eta
1	400	80	0.5	0.2	0.05	20
2	400	80	0.9	0.05	0.05	20
3	400	80	0.9	0.95	0.95	15
4	400	80	0.9	0.2	0.05	20
5	400	80	0.5	0.2	0.2	20
6	400	80	0.5	0.05	0.05	15

3. Results and discussion

3.1. Parametric analysis

Figure 6 illustrates a cross section of the design space for a heat exchanger with 260 channels and metal foam porosity of 85% showing the dependence of the objectives and recuperator performance on pore density of air and gas side. The plots provide valuable insights into the intricate relationship between the input parameters and the objectives.

The influence of pore density on the heat transfer of the recuperator is illustrated in Figure 6(a). The relationship between pore density and the overall heat transfer coefficient is non-linear due to a combination of several interconnected factors. As pore density increases, the diameter of the ligament decreases, resulting in a higher interfacial surface density and a larger conduction area, which, in turn, enhances heat transfer from the solid to the fluid medium. However, the increase in pore density also leads to the generation of tortuous flow paths, promoting mixing effects within the metal foam. Additionally, the interaction between the increased surface area and the tortuosity creates intricate interdependencies that contribute to the observed non-linear behaviour of the overall heat transfer coefficient with respect to pore density.



(a) (b)

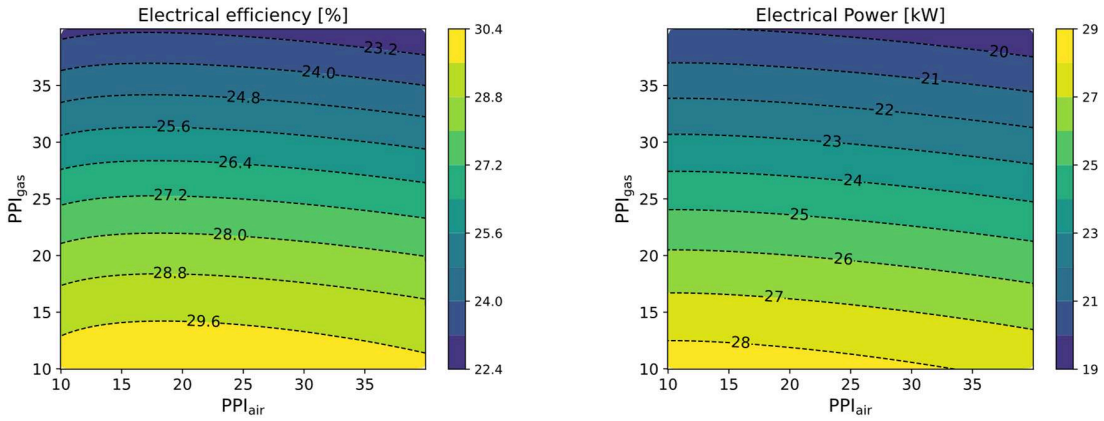


Figure 6: Design space analysis for a heat exchanger with 260 channels and metal foam porosity of 85%. (a) Overall heat transfer coefficient as a function of pore density on gas and air side; (b) total pressure drops as a function of pore density on gas and air side; (c) electrical efficiency as a function of pore density on gas and air side; (d) electrical power as a function of pore density on gas and air side.

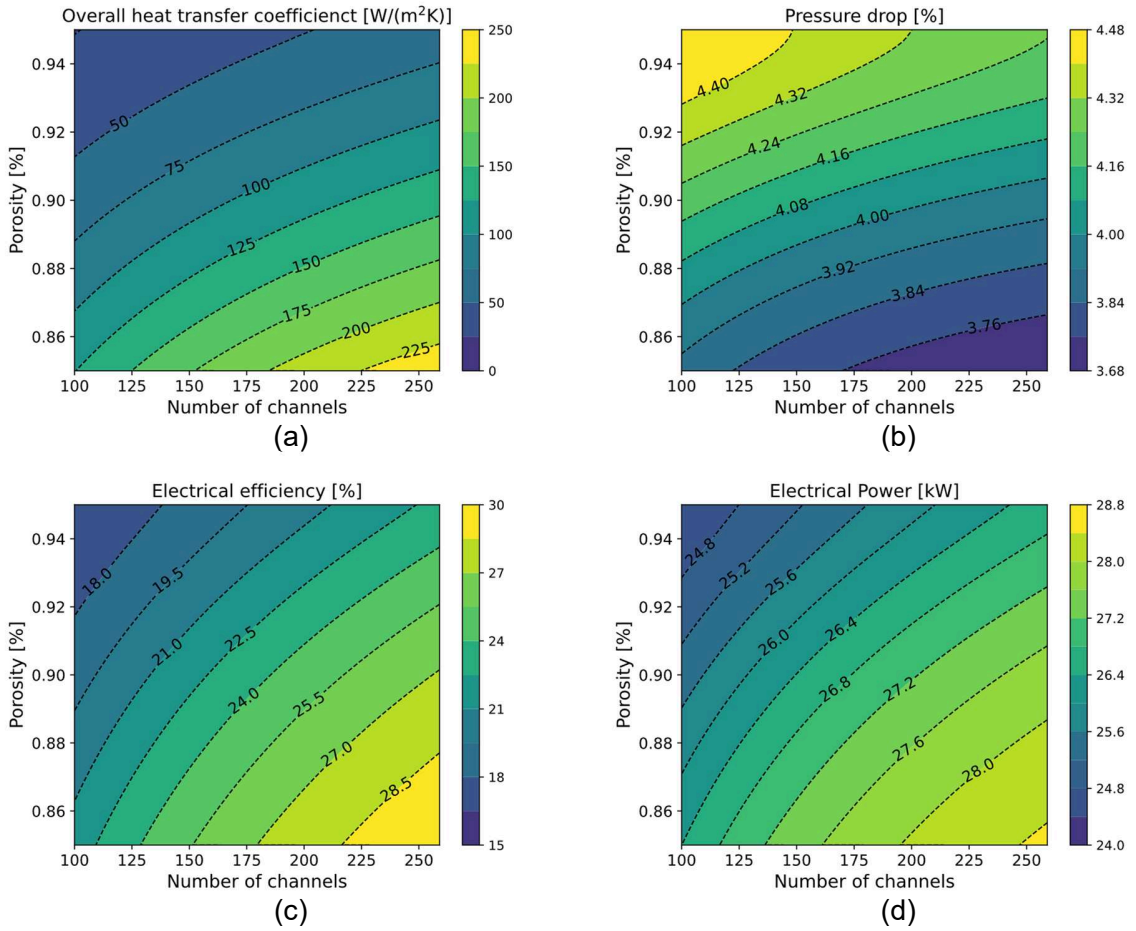
Increasing pore density in metal foams leads to a surge in pressure drop, as illustrated in Figure 6(b). Increasing pore density is the primary factor responsible for causing an increase in pressure drop, particularly on the gas side. On the gas side, the fluid is expanded so the pressure is much lower than that of the compressed air. As a result, the pressure difference is higher on the gas side and the effect of pore density on pressure drop is less pronounced on the air side. Consequently, pressure drop and heat transfer within the recuperator have counteractive effects on the overall system performance.

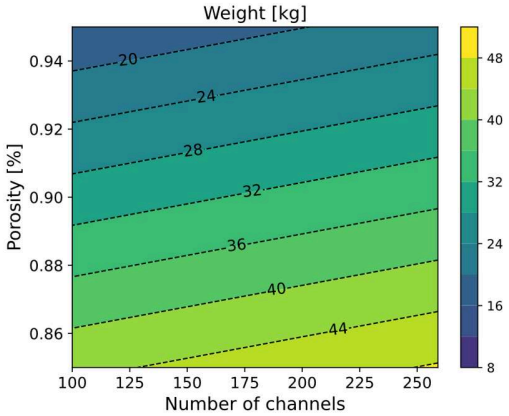
Figure 6(c) and (d) show that a rise in pressure drop resulting from a pore density increase has a more significant impact on the system performance compared to that of heat transfer. The more pronounced pressure drop on the gas side is a key factor contributing to the overall reduction in efficiency when PPI is increased on the gas side. On the air side, there is a slight enhancement of electrical efficiency at low pore density, attributed to a sharp increase in the overall heat transfer coefficient and a lower impact on pressure drop. However, beyond a pore density range of 12 to 15 PPI, the electrical efficiency starts to decline slightly, indicating that at higher values of pore density, pressure drop becomes more dominant than heat transfer.

Figure 7 depicts a cross-section of the design space for metal foam with 10 PPI on air and gas side showing the dependence of the three objectives and recuperator performance on the number of channels and porosity. Figure 7(a) shows that a reduction in foam porosity and an increase of the number of channels enhance the overall heat transfer coefficient. This occurs because reducing porosity causes the ligament diameter to increase, increasing the effective solid thermal conductivity, which is the dominant factor influencing heat transfer in metal foams. An increase in the number of channels introduces additional material that facilitates heat exchange between the two fluids. This rise in channels also increases the available surface area, resulting in an improved overall heat transfer coefficient. This improvement is weaker than that caused by porosity change.

The impact of both porosity and number of channels on pressure drop is not significant, as the resulting range of pressure drop in Figure 7(b) is low. This subtle change in pressure drop with the increase in porosity is more prominently influenced by slight variations in fluid thermophysical properties, such as density and viscosity, resulting from the impact of porosity on outlet

temperature changes. The effect of porosity is more prominent in the pressure drop rather than that of the number of channels. In porous media, pressure drop is affected primarily by foam geometry rather than channel geometry [20]. Therefore, a change of pressure drop by increasing the number of channels is caused primarily by the change of mass flow rate at each channel. Figure 7(a) and (b) suggest that porosity has a more substantial influence on recuperator overall heat transfer coefficient than on pressure drop. Figure 7(c) and (d) show that reducing the porosity improves the performance of the cycle. An increase in the overall heat transfer coefficient through porosity change enhances the effectiveness of the recuperator, leading to improvements in the power output by increasing cycle temperatures T_5 and T_3.





(e)

Figure 7: Design space and analysis for pore density of 10 PPI on both gas and air side. (a) Overall heat transfer coefficient as a function of number of channels and porosity; (b) total pressure drop as a function of number of channels and porosity; (c) electrical efficiency as a function of number of channels and porosity; (d) electrical power as a function of number of channels and porosity; (e) recuperator weight as a function of number of channels and porosity.

Pore density does not have an effect on recuperator weight, as changes in pore density only result in a change in surface area rather than a change in material density. In contrast, changes in the number of channels or porosity cause a proportional change in the weight of the recuperator resulting in straight contour lines as shown in Figure 7(e). With an increase in the number of channels, there is a slight corresponding increase in the weight of the recuperator. This relationship suggests that adding more channels adds material to the recuperator, which increases its weight. On the other hand, as porosity decreases, the weight of the recuperator increases significantly. The relationship between porosity and weight suggests that porosity plays a crucial role in determining the density and subsequently the weight of material used in the recuperator.

This analysis reveals monotonic behaviour in the results when considering porosity and the number of channels. In such cases, linear optimisation could suffice for the analysis. However, pore densities introduce non-linearities as evidenced by the local maximum shown in Figure 6a and 6c. To address these complexities use of GA is necessary to ensure robust optimisation searching multidimensional spaces with non-monotonic relationships.

3.2. Multi-objective optimisation

3.2.1. Reliability testing

The reliability, robustness, and reproducibility of NSGA-II are assessed in Table 4 presenting the performance indicator between pairs of Pareto fronts. This table shows the results for the 6 runs summarised in Table 3. The Pareto front from each run is compared against a theoretical Pareto front (TPF) from the exhaustive search using 200,000 points and 300,000 points. All runs reveal that the theoretical pareto front calculated from 200,000 points is coarser than that from 300,000 points. For the 300,000 points, the mean performance indicator of the 6 runs outperforms the coarser search by 52% indicating the high computational cost when executing the optimisation using exhaustive search. The algorithm achieves a solution using a significantly more efficient method, with a computational time of 3.8 hours, requiring only 10% of computational resources

compared to the exhaustive search. The exhaustive search, on the other hand, would require the inclusion of over 300,000 data points to attain a comparable level of precision. This highlights the algorithm effectiveness in efficiently exploring the solution space and identifying high-quality solutions. Such efficiency makes NSGA-II a preferred choice for tackling multi-objective optimisation tasks, especially when exhaustive search is infeasible due to the problem high dimensionality and complexity. Furthermore, a comparison is made between the Pareto front of the last generation and the Pareto fronts from different generations of each run, aiming to assess the convergence of the algorithm based on the specified termination criteria. NSGA-II approximates the Pareto set at 400 generations with a population of 80 thereby confirming the validity of the chosen termination criteria. The algorithm reproducibility was examined by employing different random seeds to generate the initial population. The Pareto fronts of the different seeds are compared against a theoretical Pareto front produced from exhaustive search of 300,000 points. The reproducibility of the solution demonstrates satisfactory consistency across the six runs.

Table 4 Performance indicator for reliability testing of NSGA-II.

Performance Indicator GD							
Run	Gen 5	Gen 10	Gen 399	TPF Seed1 200,000 points	TPF Seed1 300,000 points	TPF Seed2 300,000 points	TPF Seed3 300,000 points
1	1.23	0.81	0.063	0.237	0.151	0.172	0.151
2	1.84	0.84	0.071	0.242	0.164	0.155	0.168
3	1.74	0.85	0.040	0.237	0.165	0.143	0.137
4	1.54	0.77	0.038	0.246	0.163	0.146	0.168
5	1.50	0.85	0.063	0.251	0.159	0.154	0.158
6	1.49	0.74	0.077	0.231	0.151	0.168	0.155

Figure 8 and Figure 9 illustrate the reliability testing outcomes. Figure 8 shows the reproducibility of the first run as the variations in the selected run reveal the difference from seed to seed. The algorithm consistently reaches the final front when initialised with different seeds. This also proves that the rest runs are reproducible as they have similar performance indicators listed in Table 4. The visualisation of convergence is shown in Figure 9. The methodology effectively approximates the Pareto Front (PF), displaying satisfactory convergence within 100 generations and reaching a closely aligned state by the 400th generation. This consistent performance is observed across different levels of complexity, showcasing the methodology robustness in various parameters.

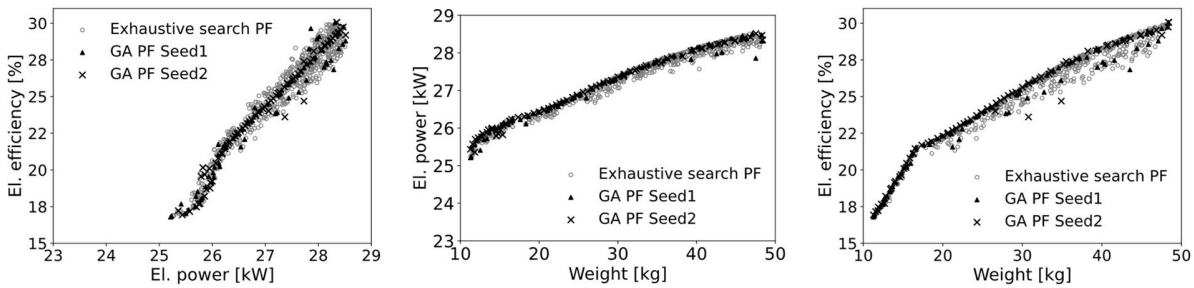


Figure 8: 2D illustrations of three objectives: Pareto front with different seeds of run 1 in comparison with pareto front calculated from exhaustive search.

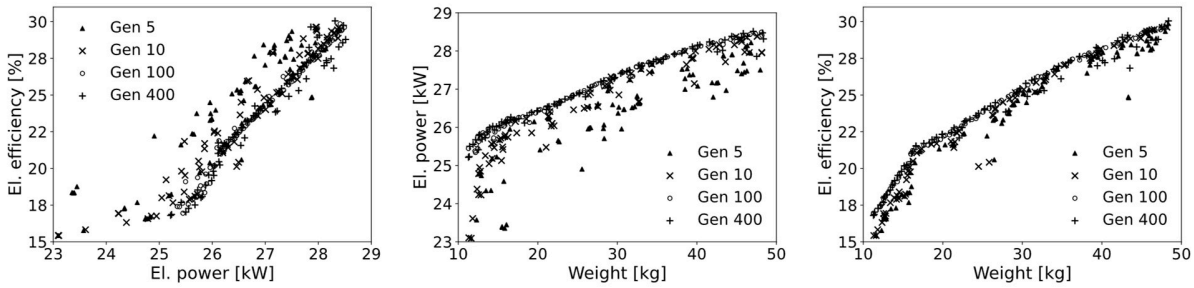
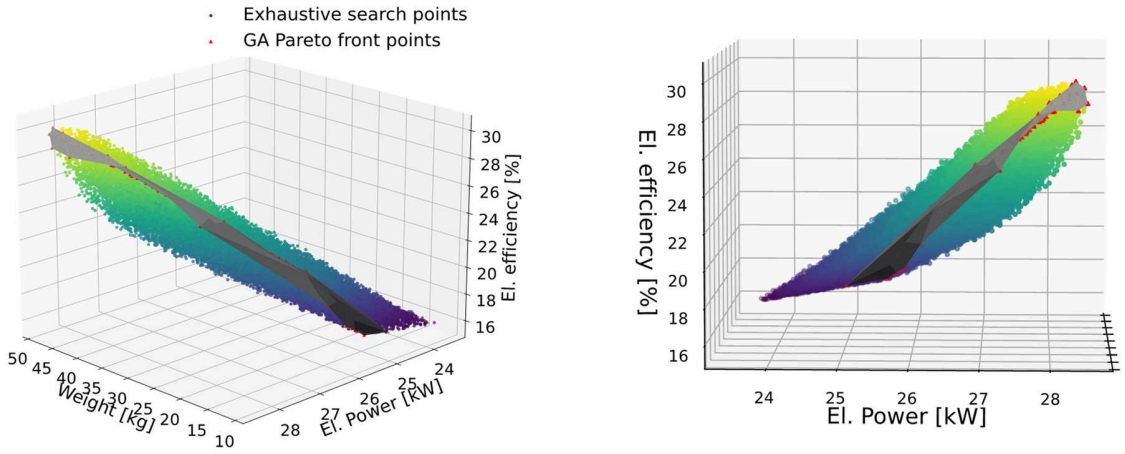


Figure 9 2D illustrations of three objectives: Pareto front at different generations of run 1.

3.2.2. Optimisation analysis

The efficiency of the GA is assessed by comparing its results with the outcome of an exhaustive search in Figure 10. The exhaustive search has been completed by randomly sampling the four-dimensional parameter space of the optimisation problem, generating 300,000 points for evaluation. Analysis from section 3.1. reveals that any changes in design parameters have a consistent impact on both efficiency and power. For instance, modifications such as increasing porosity or pore density cause a decrease in both power output and electrical efficiency. Conversely, increasing the number of channels results in an increase in both power output and electrical efficiency. This relationship is reflected in the 3D isometric view of Figure 10, where the shape of the surface signifies that as power output increases, efficiency also increases. Likewise, the cloud of exhaustive search points shows that recuperator weight rises with an increase in the other two objectives. The GA Pareto front includes all the optimal solutions present in the objective space. Each solution is characterised by a unique and specific recuperator geometry corresponding to a unique set of parameters.



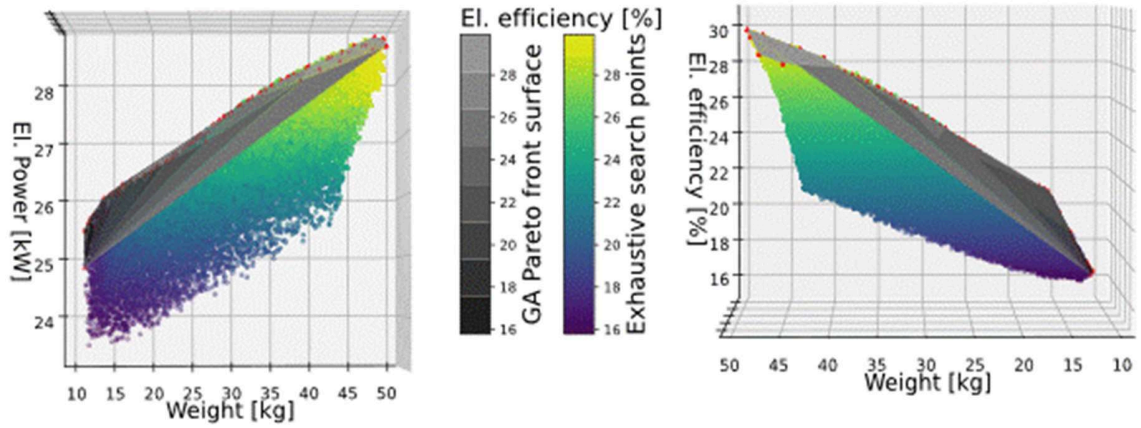


Figure 10: Pareto set surface plot on GA pareto front points and exhaustive search points comparison: different views of 3D plot.

Figure 11 presents a comparison between the Pareto front calculated by NSGA-II, the Pareto front from exhaustive search and the points of the exhaustive search. It illustrates a 2D projection of the points in Figure 10, showing that the GA reaches a Pareto set that slightly outperforms the exhaustive search due to the effective finer resolution of the algorithm compared to the search. The NSGA-II algorithm achieves its solution using a maximum of only 10% of the function evaluation and computation effort that would be required for an exhaustive search of equivalent outputs.

Figure 11(a) illustrates the relation between electrical efficiency and power output and compares the results of multi-objective optimisation with the solution of the C30 design. This design is a baseline case that represents the industry standard. According to specifications it is rated to 29 kW with 26% efficiency and 0.31 mass flow rate on the gas side [47]. In general, the result show that these two objectives are correlated, suggesting that there is a less significant trade-off between them, and it is possible to achieve improvements in both simultaneously. The change in slope of the Pareto front above 26 kW of power indicates that optimisation results are governed by the constraints. The initial steeper slope indicates that there is a relatively small trade-off between the objectives. Above 26 kW, the gradient is reduced, indicating that further improvements in the first objective are associated with greater variation of the second objective. These designs showcase improved efficiency without any reduction in power output when compared to industry standards, which typically are around 26%. Also observing the plot in Figure 11(b), the optimum solutions comparable with recuperators in the market such as Capstone C30 can be achieved at a weight less than 50 kg with the same external dimensions. By utilizing the corresponding optimal design parameters, the calculated effectiveness reaches approximately 85%. The corresponding core weight, excluding auxiliary parts, is 32 kg, resulting in a specific weight of 103 kg/(kg s). This value falls within the range of Mc Donald's charts for 85% effectiveness [3]. This comparison with a compact recuperator for μ-GTs indicates that the use of metal foam in heat exchangers is viable for the improvement of performance of a μ-GT. Furthermore, in terms of weight, the proposed designs represent a state-of-the-art solution. The curve with a positive gradient in Figure 11(b) suggests a trade-off between the power output and weight. There is a linear trade-off, where the rate of change in weight is proportional to the rate of change in power output with an average sensitivity of 0.08 kW/kg. This signifies a consistent and predictable relationship between the two objectives.

Figure 11(c) presents the relation between electrical efficiency and recuperator weight. In the low weight region of Pareto front, the gradient is greater, indicating that there is significant margin for improvement in maximising efficiency by incurring a penalty in recuperator weight. This region reflects a relatively favourable trade-off between the objectives, allowing substantial gains in efficiency without compromising weight to a large extent. However, moving to the greater weight region, the front becomes less steep, indicating a greater penalty in weight for improving efficiency. Within this region, further enhancement in efficiency comes at a higher cost in terms of increasing weight. Balancing the two objectives becomes more challenging. This transition could arise due to limitations of design space inherent to the problem.

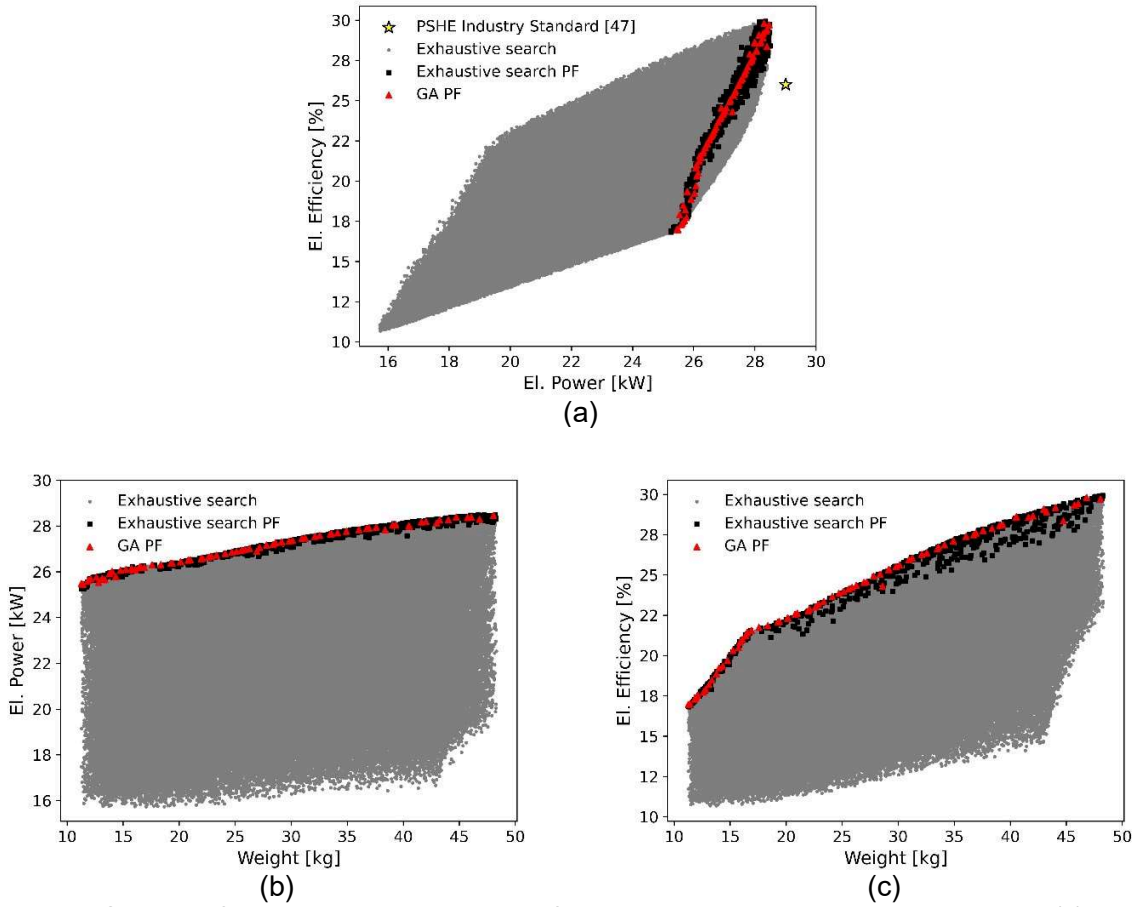


Figure 11: GA Pareto front, Exhaustive search pareto front and exhaustive search points comparison. (a) 2D view of electrical efficiency vs power output, compared with C30 point; (b) 2D view of power output vs recuperator weight and (c) 2D view of electrical efficiency vs recuperator weight.

3.3. Validation and off-design analysis

The Pareto set achieved through the NSGA-II optimisation is utilised to create a curve representing the relationship between electrical efficiency and the effectiveness of a metal foam recuperator, as shown in Figure 13. This relationship is validated against a study that uses a recuperator with multiple channels and the same thermodynamic model as this work [60]. To ensure a fair comparison, the mass flow rate is adjusted to yield an 8 kW power output. The observed trends reveal a similar second-order polynomial curve. The metal foam solution exhibits

a favourable performance below 90% recuperator effectiveness. In contrast, the design from [60] demonstrates a steeper gradient beyond this threshold, showcasing higher efficiency within the 90-95% effectiveness range. This divergence could be attributed to the specific metal foam geometry features, accentuating the trade-off between effectiveness and efficiency in the present study. As detailed in section 3.1 enhanced heat transfer achieved by high pore densities, results in high metal foam area and effectiveness. However, it is important to maintain optimal pore densities below 20 PPI to prevent efficiency deterioration due to increase in pressure drop.

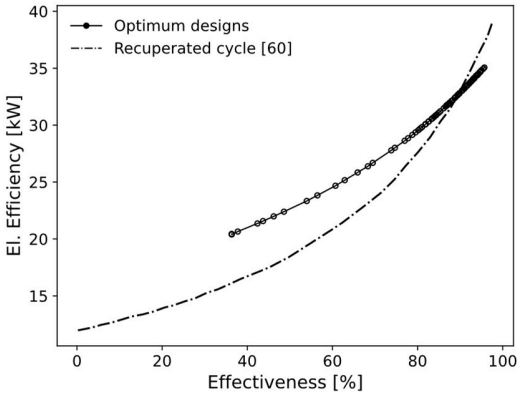


Figure 12: Thermodynamic model validation with a concept multiple channel recuperator [60] proving impact of effectiveness on cycle efficiency

By utilising the numerically calculated temperatures and employing the electrical efficiency formula, the cycle efficiency of the unrecuperated engine was calculated to be 16.3% at the design point. The efficiency of the μ-GT improves when the effectiveness of the recuperator exceeds 10%. The curve becomes steeper beyond the 60% effectiveness threshold, resulting in even greater improvement. Furthermore, as the effectiveness approaches 90%, the efficiency nearly doubles compared to the initial level. Figure 13 (b) compares the performance of two optimised designs, Case 1, and Case 2, under off-design conditions. The selection of these cases is driven by distinct emphasis on specific performance metrics: Case 1 is optimised for higher efficiency, whereas Case 2 prioritises different factors, such as weight reduction, despite a trade-off with lower efficiency and power. A mass flow rate range is considered between $0.5\ \dot{\boldsymbol{m}}_{\boldsymbol{air}}$ to $2\ \dot{\boldsymbol{m}}_{\boldsymbol{air}}$ as off-design conditions. The two curves depict the impact of the resulting power output on efficiency. Increasing the mass flow rate correlates with a rise in power output, attributed to a greater supply of fuel and oxygen for combustion, consequently elevating the turbine inlet temperature. However, this increase in mass flow rate leads to a reduction in system efficiency. High flow rate limits the residence time of working fluids in the recuperator, reducing heat transfer. This decrease results in reduced recuperator effectiveness, causing a reduction in temperature difference and, subsequently, a decrease in cycle efficiency. Furthermore, higher mass flow rates can lead to increased pressure drop across the recuperator. As seen Figure 6 (b), (c), and (d), pressure drop affects significantly the system efficiency and power. The two slightly divergent curves in Figure 13 (b) indicate that the efficiency penalty in the first case is lower than the second case as indicated by the lower slope. This outcome is attributed to the differences in geometric parameters between the two different designs. Thus, the superior performance of case 1 is evident not only at the design point resulting in higher efficiency and power, but also extends the off-design conditions, showcasing a superior performance for the μ-GT.

Prioritising efficiency and power over weight, Case1 is the preferred choice at the design point. In addition, the performance response of Case 1 at off-design conditions aligns with an acceptable range for this geometry. Case 1 achieves efficiency of 30.1% and power output of 28.3 kW, whereas in C30, the values are 26% and 29 kW respectively. The efficiency improvement over the industry standard is 15% with only 2.5 % reduction in power output.

The details of these two designs are summarised in Table 5. The results highlight the differences in performance and characteristics between the two recuperator designs for the μ-GT. Case 1 generally demonstrates superior heat transfer, effectiveness, power output, and electrical efficiency, but it also comes with a greater weight and larger total area requirement. The similar total pressure drop observed in the two cases can be attributed to trade-offs in various design parameters. Specifically, the higher pore density on the air side, lower porosity, and increased number of channels contribute to balancing the pressure drop. These design choices influence the flow resistance and overall pressure drop, resulting in comparable values between the two cases. Additionally, a high overall heat transfer coefficient of 272.5 W/m^2 K is achieved due to the combination of a high foam area and a low heat exchange area of 7.25 m^2, which eliminates the need for costly production of corrugations.

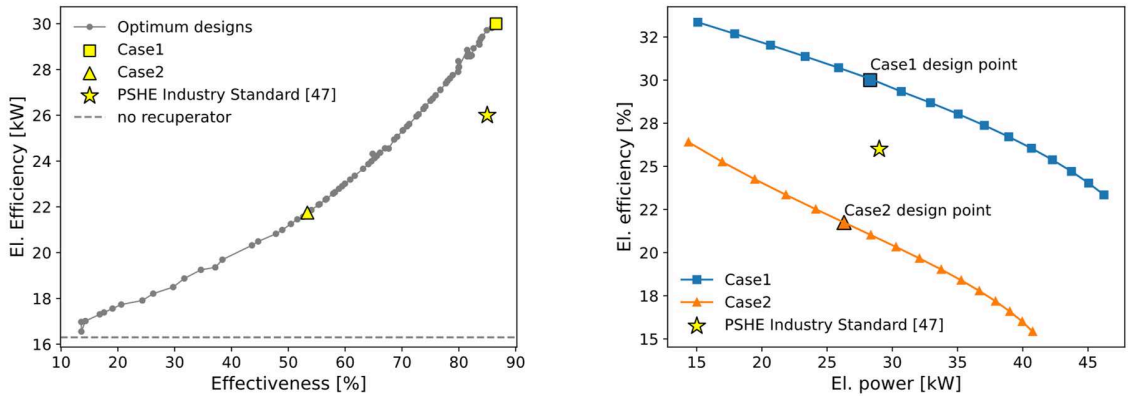


Figure 13: Effect of recuperator on cycle performance and temperatures. (a) Influence of recuperator effectiveness on cycle efficiency; (b) off-design performance analysis: impact of heat exchanger design on micro gas turbine efficiency and power output for optimised geometries, case 1 and case 2.

Table 5 Numerical results for two optimised recuperator geometries

Performance parameter	Case 1	Case 2
PPI_{air}	21	10
PPI_{gas}	9.98	10
Porosity	0.85	0.97
Number of channels	260	260
Effectiveness (%)	86.5	53
Nu_{air}	84.5	13.24
Nu_{gas}	63.3	13.48
Overall heat transfer coefficient (W/m^{2}K)	272.5	49.3
Pressure drop (%)	4.11	4.15

Heat exchange area (m^2)	7.25	7.23
Total recuperator area (m^2)	61.88	24
Weight (kg)	48.4	17.6
Power output (kW)	28.34	26.3
Electrical efficiency (%)	30.06	21.8

4. Conclusions

This study has explored the potential of metal foam technology in enhancing the performance of μ-GTs. By leveraging the unique thermal properties of metal foam in a recuperator, heat transfer performance, pressure drop, weight, power output and electrical efficiency gain have been successfully quantified in a multi-objective optimisation problem. The optimisation process, carried out using the NSGA-II algorithm, identified an optimal set of design parameters that directly affect the cycle efficiency, power output, and recuperator weight. Based on the results from the parametric study and the algorithm evaluation, the following conclusions can be inferred:

- Both macro-scale and micro-scale geometrical features of metal foam recuperator have an impact on the cycle efficiency of the system. A higher number of channels corresponds to improved power output and electrical efficiency while also resulting in elevated weight. However, the impact of number of channels in the overall performance is not as high as the impact of pore density on the gas side and porosity.
- Under the examined range of porosity, heat transfer is increased when porosity decreases, but the impact in recuperator weight is considerable. This also results in both power output and electrical efficiency increasing, maximised at 85% porosity.
- Due to the high pore density, the enhanced surface raises the overall exchanger heat transfer coefficient but the effect on pressure drop is detrimental. Although initial improvement on efficiency on low pore density is observed, as soon as the efficiency reaches the optimum set of values, any pore density increase, leads to further pressure drop which becomes the driving variable for the decrease of efficiency. The optimum set of pore densities is 10 PPI for gas side, and 20 for air side.
- The NSGA-II algorithm is preferred over an exhaustive search, as it produces a refined Pareto front at a computational cost at a maximum of 10% of the exhaustive search.

The results highlight the optimum combination of design parameters for a light weight and compact recuperator that overcome the impediment of material cost and manufacturing flexibility is favourable. A new generation of metal foam channels is introduced in a μ-GT recuperator and can achieve electrical efficiency of 30 %, maintaining a state-of-the-art weight of 48 kg. The efficiency improvement over the industry standard is 15% with only 2.5 % reduction in power output. The results of this study can motivate future work for manufacturing the optimum designs proposed and to allow experimental investigation of the system performance and a more comprehensive validation. The vision generated from this work is to evolve μ-GTs through the integration of innovative metal foam technology in the recuperator. Advancements of this technology will have a positive impact on sustainable and environmentally friendly power generation.

Acknowledgments

This project has received funding from the European Union's Horizon 2020 research and innovation programme under Marie Sklodowska-Curie grant agreement No 861079.

CRediT author statement

Panagiota Chatzi: Conceptualisation, Methodology, Data curation, Writing – original draft, **Theofilos Efstathiadis**: Funding acquisition, **Alex Skordos**: Conceptualisation, writing – review and editing, **Anestis Kalfas**: Supervision

References

[1] J. E. Hesselgreaves, R. Law and D. Reay, Compact Heat Exchangers: Selection, Design and Operation, Butterworth-Heinemann, 2016.

[2] A. Aquaro and D. Pieve, "High temperature heat exchangers for power plants: Performance of advanced metallic recuperators," Applied Thermal Engineering, vol. 27, no. 2-3, pp. 389-400, 2007. https://doi.org/10.1016/j.applthermaleng.2006.07.030

[3] C. F. McDonald, "Recuperator considerations for future higher efficiency microturbines," Applied Thermal Engineering, vol. 23, pp. 1463-1487, 2003. https://doi.org/10.1016/S1359-4311(03)00083-8

[4] K. Bollas, T. Efstathiadis and A. I. Kalfas, "Deterministic Optimisation Approach for High-Performance Externally-Fired Biomass-Fueled Micro-Gas Turbines," Journal of Engineering for Gas Turbines and Power, pp. 1-34, 2023. https://doi.org/10.1115/1.4062479

[5] C. F. McDonald and D. G. Wilson, "The utilization of recuperated and regenerated engine cycles for high-efficiency gas turbines in the 21st century," Applied Thermal Engineering, vol. 16, no. 8-9, pp. 635-653, 1996. https://doi.org/10.1016/1359-4311(95)00078-X

[6] C. F. McDonald, "Low Cost Recuperator Concept for Microturbine Applications," in ASME Turbo Expo 2000, Munich, 2000. https://doi.org/10.1115/2000-GT-0167

[7] E. Utriainen and B. Sunden, "Evaluation of the Cross Corrugated and Some Other Candidate Heat Transfer Surfaces for Microturbine Recuperators," Journal of Engineering for Gas Turbines and Power, vol. 124, no. 3, pp. 550-560, 2002. https://doi.org/10.1115/1.1456093

[8] P. Hafeez, L. Esmaeelpanah, S. Chandra and J. Mostaghimi, "Heat Transfer Through Metal-Foam Heat Exchanger at Higher Temperature," in ASME, Minneapolis, 2013. https://doi.org/10.1115/HT2013-17775

[9] P. M. Kamath, C. Balaji and S. P. Venkateshan, "Convection heat transfer from aluminium and copper foams in a vertical channel – An experimental study," International Journal of Thermal Sciences, vol. 64, pp. 1-10, 2013. https://doi.org/10.1016/j.ijthermalsci.2012.08.015

[10] B. Treece and R. McKeirnan, “Microturbine Recuperator Manufacturing and Operating Experience,” in ASME, Amsterdam, 2002. https://doi.org/10.1115/GT2002-30404

[11] X. Chen, X. Xia, C. Sun, F. Wang and R. Liu, “Performance evaluation of a double-pipe heat exchanger with uniform and graded metal foams,” Heat and Mass Transfer, vol. 56, pp. 291-302, 2020. https://doi.org/10.1007/s00231-019-02700-3

[12] K. Nawaz, J. Bock and A. M. Jacobi, “Thermal-hydraulic performance of metal foam heat exchangers under dry operating conditions,” Applied Thermal Engineering, vol. 119, pp. 222-232, 2017. https://doi.org/10.1016/j.applthermaleng.2017.03.056

[13] S. Mancin, C. Zilio, A. Cavallini and L. Rossetto, “Heat transfer during air flow in aluminium foams,” International Journal of Heat and Mass Transfer, vol. 53, p. 4976–4984, 2010. https://doi.org/10.1016/j.ijheatmasstransfer.2010.05.033

[14] S. Mancin, C. Zilio, A. Diani and L. Rossetto, “Air forced convection through metal foams Experimental results and modeling,” International Journal of Heat and Mass Transfer, vol. 62, pp. 112-123, 2013. https://doi.org/10.1016/j.ijheatmasstransfer.2013.02.050

[15] T. H. Kim, W. Lee and J. H. Jeong, “Thermo-fluidic characteristics of open cell metal foam as an anodes for DCFC, part I: Head loss coefficient of metal foam,” International Journal of Hydrogen Energy, vol. 39, no. 23, pp. 12369-12376, 2014. https://doi.org/10.1016/j.ijhydene.2014.03.075

[16] G. S. Beavers and E. M. Sparrow, “Non-Darcy Flow Through Fibrous Porous Media,” Journal of Applied Mechanics, vol. 36, no. 4, pp. 711-714, 1969. https://doi.org/10.1115/1.3564760

[17] H. Wang and L. Guo, “Experimental investigation on pressure drop and heat transfer in metal foam filled tubes under convective boundary condition,” Chemical Engineering Science, vol. 155, pp. 438-44, 2016. https://doi.org/10.1016/j.ces.2016.08.031

[18] B. Dietrich, W. Schabel, M. Kind and H. Martin, “Pressure drop measurements of ceramic sponges—Determining the hydraulic diameter,” Chemical Engineering Science, vol. 64, no. 16, pp. 3633-3640, 2009. https://doi.org/10.1016/j.ces.2009.05.005

[19] E. A. Moreira, M. D. M. Innocentini and J. R. Coury, “Permeability of ceramic foams to compressible and incompressible flow,” Journal of the European Ceramic Society, vol. 24, no. 10-11, pp. 3209-3218, 2004. https://doi.org/10.1016/j.jeurceramsoc.2003.11.014

[20] C. Y. Zhao, T. Kim, T. J. Lu and H. P. Hodson, “Thermal Transport in High Porosity Cellular Metal Foams,” Journal of Thermophysics and Heat Transfer, vol. 18, no. 3, 2004. https://doi.org/10.2514/1.11780

[21] H. J. Xu, Z. G. Qu and W. Q. Tao, “Thermal transport analysis in parallel-plate channel filled with open-celled metallic foams,” International Communications in Heat and Mass Transfer, vol. 38, p. 868–873, 2011. https://doi.org/10.1016/j.icheatmasstransfer.2011.04.015

[22] K. Boomsma and D. Poulikakos, “Metal foams as compact high performance heat exchangers,” Mechanics of Materials, vol. 35, no. 12, pp. 1161-1176, 2003. https://doi.org/10.1016/j.mechmat.2003.02.001

[23] S. Y. Kim, J. W. Paek and B. H. Kang, “Flow and heat transfer correlations for porous fin in a plate-fin heat exchanger,” Journal of Heat Transfer, vol. 122, pp. 572-578, 2000. https://doi.org/10.1115/1.1287170

[24] S. Y. Kim, B. H. Kang and J. Kim, “Forced convection from aluminum foam materials in an asymmetrically heated channel,” International Journal of Heat and Mass Transfer, vol. 44, pp. 1451-1454, 2001. https://doi.org/10.1016/S0017-9310(00)00187-3

[25] W. Lu, C. Y. Zhao and S. A. Tassou, “Thermal analysis on metal-foam filled heat exchangers. Part I: Metal-foam filled pipes,” International journal of heat and mass transfer, vol. 49, no. 15-16, pp. 2751-2761, 2006. https://doi.org/10.1016/j.ijheatmasstransfer.2005.12.01

[26] C. Y. Zhao, W. Lu and S. A. Tassou, “Thermal analysis on metal-foam filled heat exchangers. Part II: Tube heat exchangers,” International Journal of Heat and Mass Transfer, vol. 49, no. 15-16, pp. 2762-2770, 2006. https://doi.org/10.1016/j.ijheatmasstransfer.2005.12.014

[27] T. Fiedler , R. Moore and N. Movahedi, “Manufacturing and Characterization of Tube-Filled ZA27 Metal Foam Heat Exchangers,” Metals, vol. 11, no. 8, 2021. https://doi.org/10.3390/met11081277

[28] T. Chen, G. Shu, H. Tian, T. Zhao, H. Zhang and Z. Zhang, “Performance evaluation of metal-foam baffle exhaust heat exchanger for waste heat recovery,” Applied Energy, vol. 266, 2020. https://doi.org/10.1016/j.apenergy.2020.114875

[29] Z. Dai, K. Nawaz, Y. Park, Q. Chen and A. Jacobi, “A comparison of metal-foam heat exchangers to compact multilouver designs for air-side heat transfer applications,” Heat transfer engineering, vol. 33, no. 1, pp. 21-30, 2012. https://doi.org/10.1080/01457632.2011.584812

[30] N. Michailidis, F. Stergioudi and D. N. Tsipas, “Manufacturing of Open-Cell Metal Foams Using a Novel Leachable Pattern,” Advanced Engineering Materials, vol. 13, no. 1-2, 2011. https://doi.org/10.1002/adem.201000141

[31] G. Bianchi, S. Gianella and A. Ortona, “Design and additive manufacturing of periodic ceramic architectures,” Journal of Ceramic Science and Technology, 2017. DOI: 10.4416/JCST2016-00088

[32] J. Y. Ho, K. C. Leong and T. N. Wong, “Additively-manufactured metallic porous lattice heat exchangers for air-side heat transfer enhancement,” International Journal of Heat and Mass Transfer, vol. 150, 2020. https://doi.org/10.1016/j.ijheatmasstransfer.2019.119262

[33] M. A. Arie, A. H. Shooshtari, V. V. Rao, S. V. Dessiatoun and M. M. Ohadi, “Air-Side Heat Transfer Enhancement Utilizing Design Optimization and an Additive Manufacturing Technique,” Journal of Heat Transfer, vol. 139, no. 3, 2017. https://doi.org/10.1115/1.4035068

[34] X. Zhang, R. Tiwari, A. H. Shoushtari and M. M. Ohadi, “An additively manufactured metallic manifold-microchannel heat exchanger for high temperature applications,” Applied Thermal Engineering, vol. 143, pp. 899-908, 2018. https://doi.org/10.1016/j.applthermaleng.2018.08.032

[35] M. Imran, N. A. Pambudi and M. Farooq, “Thermal and hydraulic optimization of plate heat exchanger using multi objective genetic algorithm,” Case Studies in Thermal Engineering, vol. 10, pp. 570-578, 2017. https://doi.org/10.1016/j.csite.2017.10.003

[36] H. Safikhani and S. Eiamsa-ard , “Pareto based multi-objective optimization of turbulent heat transfer flow in helically corrugated tubes,” Applied Thermal Engineering, vol. 95, pp. 275-280, 2016. https://doi.org/10.1016/j.applthermaleng.2015.11.033

[37] S. Chamoli, p. Yu and S. Yu, “Multi-objective shape optimization of a heat exchanger tube fitted with compound inserts,” Applied Thermal Engineering, vol. 117, pp. 708-724, 2017. https://doi.org/10.1016/j.applthermaleng.2017.02.047

[38] M. Siavashi, H. R. T. Bahrami and E. Amnian, “Optimization of heat transfer enhancement and pumping power of a heat exchanger tube using nanofluid with gradient and multi-layered porous foams,” Applied Thermal Engineering, vol. 117, pp. 465-474, 2018. https://doi.org/10.1016/j.applthermaleng.2018.04.066

[39] Y. Ge, Z. Liu and W. Liu, “Multi-objective genetic optimization of the heat transfer for tube inserted with porous media,” International Journal of Heat and Mass Transfer, vol. 101, pp. 981-987, 2016. https://doi.org/10.1016/j.ijheatmasstransfer.2016.05.118

[40] Z. Zheng, M. Li and Y. He, “Optimization of porous insert configurations for heat transfer enhancement in tubes based on genetic algorithm and CFD,” International Journal of Heat and Mass Transfer, vol. 87, pp. 376-379, 2015. https://doi.org/10.1016/j.ijheatmasstransfer.2015.04.016

[41] S. Du, Y. He, W. Yang and Z. Liu, “Optimization method for the porous volumetric solar receiver coupling genetic algorithm and heat transfer analysis,” International Journal of Heat and Mass Transfer, vol. 122, pp. 383-390, 2018. https://doi.org/10.1016/j.ijheatmasstransfer.2018.01.120

[42] S. Du, Q. Ren and Y. He, “Optical and radiative properties analysis and optimization study of the gradually-varied volumetric solar receiver,” Applied Energy, vol. 207, pp. 27-35, 2017. https://doi.org/10.1016/j.apenergy.2017.05.165

[43] N. Bianco, S. Busiello, M. Iasiello and G. M. Mauro, “Finned heat sinks with phase change materials and metal foams: Pareto optimization to address cost and operation time,” Applied Thermal Engineering, vol. 197, no. 117436, 2021.

https://doi.org/10.1016/j.applthermaleng.2021.117436

[44] N. Bianco, M. Iasiello, G. M. Mauro and L. Pagano, “Multi-objective optimization of finned metal foam heat sinks: Tradeoff between heat transfer and pressure drop,” Applied Thermal Engineering, vol. 182, no. 116058, 2021. https://doi.org/10.1016/j.applthermaleng.2020.116058

[45] G. Xiao, T. Yang, H. Liu, N. Dong, M. Ferrari, M. Li, Z. Luo, K. Cen and M. Ni, “Recuperators for micro gas turbines: A review,” Applied Energy, vol. 197, pp. 83-99, 2017. https://doi.org/10.1016/j.apenergy.2017.03.095

[46] J. Cai, X. Huai and W. Xi, “An optimal design approach for the annular involute-profile cross wavy primary surface recuperator in microturbine and an application case study,” Energy, vol. 153, pp. 80-89, 2018. https://doi.org/10.1016/j.energy.2018.04.016

[47] A. Gimelli and R. Sannino, “Thermodynamic model validation of Capstone C30 micro gas turbine,” Energy Procedia, vol. 126, pp. 955-962, 2017. https://doi.org/10.1016/j.egypro.2017.08.184

[48] I. H. Bell, J. Wronski, S. Quoilin and V. Lemort, “Pure and Pseudo-pure Fluid Thermophysical Property Evaluation and the Open-Source Thermophysical Property Library CoolProp,” Industrial \& Engineering Chemistry Research, vol. 53, no. 6, pp. 2498-2508, 2014. https://doi.org/10.1021/ie4033999

[49] S. S. Feng, J. J. Kuang, T. Wen, T. J. Lu and K. Ichimiya, “An experimental and numerical study of finned metal foam heat sinks under impinging air jet cooling,” International Journal of Heat and Mass Transfer, vol. 77, pp. 1063-1074, 2014. https://doi.org/10.1016/j.ijheatmasstransfer.2014.05.053

[50] D. Lee and K. Vafai, “Analytical characterization and conceptual assessment of solid and fuid temperature differentials in porous media,” International Journal of Heat and Mass Transfer, vol. 42, pp. 423-435, 1999. https://doi.org/10.1016/S0017-9310(98)00185-9

[51] A. Zukauskas, “Heat Transfer from Tubes in Crossfow,” Advances in Heat Transfer, vol. 8, pp. 93-160, 1972. https://doi.org/10.1016/S0065-2717(08)70038-8

[52] V. V. Calmidi, “Transport Phenomena in High Porosity Fibrous Metal Foams,” Ph.D. thesis,, University of Colorado, Boulder, CO, 1998.

[53] K. Boomsma and D. Poulikakos, “On the Effective Thermal Conductivity of a Three Dimensionally Structured Fluid Saturated Metal Foam,” International Journal of Heat and Mass Transfer, vol. 44, p. 827–836, 2001. https://doi.org/10.1016/S0017-9310(00)00123-X

[54] S. Mancin, C. Zilio, A. Cavallini and L. Rossetto, “Pressure drop during air flow in aluminum foams,” International Journal of Heat and Mass Transfer, vol. 53, pp. 3121-3130, 2010. https://doi.org/10.1016/j.ijheatmasstransfer.2010.03.015

[55] G. Taylor, O. Yeo and P. Young, “CFD simulation of flow through an open cell foam,” International Journal of Modern Physics C, vol. 19, no. 5, pp. 703-715, 2008.

[56] D. G. Goodwin, H. K. Moffat and I. Schoegl, “Cantera: An object-oriented software toolkit for chemical kinetics, thermodynamics, and transport processes,” Version 2.6.0., 2022. [Online]. Available: https://www.cantera.org.

[57] J. Blank and K. Deb, “pymoo: Multi-Objective Optimization in Python,” IEEE Access, vol. 8, pp. 89497-89509, 2020. DOI: 10.1109/ACCESS.2020.2990567

[58] K. Dep, A. Pratap, S. Agarwal and T. Meyarivan, “A fast and elitist multiobjective genetic algorithm: NSGA-II,” IEEE Transactions on Evolutionary Computation, vol. 6, no. 2, pp. 182-197, 2002. DOI: 10.1109/4235.996017

[59] G. Struzziero and A. A. Skordos, “Multi-objective infusion optimization in vacuum assisted resin transfer moulding (VARTM) using genetic algorithms.,” in InICCM19-19th International conference on composite materials., Montreal, Canada, 2013. DOI: 10.13140/2.1.2085.9689

[60] J. L. Cordova, J. Walton and H. Heshmat, “High Effectiveness, Low Pressure Drop Recuperator for High Speed and Power Oil-Free Turbogenerator,” in ASME Turbo Expo, Montreal, Quebec, Canada, 2015. https://doi.org/10.1115/GT2015-43718



https://dspace.org/

Metal foam recuperators on micro gas turbines: Multi-objective optimisation of efficiency, power and weight

Chatzi, Panagiota; Efstathiadis, Theofilos; Skordos, Alexandros A.; Kalfas, Anestis I.

2024-04-01
Elsevier
https://doi.org/10.1016/j.applthermaleng.2024.122410
Chatzi P, Efstathiadis T, Skordos AA, Kalfas AI. (2024) Metal foam recuperators on micro gas turbines: Multi-objective optimisation of efficiency, power and weight. Applied Thermal Engineering, Volume 242, April 2024, Article number 122410

Downloaded from a DSpace repository. https://dspace.org/